Study of Thermal Stresses Developed during a Fatigue Test on an Electrical Motor Rotor Cage

Vicente Climente-Alarcon*
Dept. of Materials Science and Metallurgy, University of Cambridge, Cambridge, UK, email: vc363@cam.ac.uk
Telf: +44 (0) 1223 76 79 33

Antero Arkkio
Dept. of Electrical Engineering and Automation, Aalto University, Espoo, FINLAND, email: antero.arkkio@aalto.fi

Jose Antonino-Daviu
Instituto Tecnológico de la Energía, ITE, Universitat Politècnica de València, Valencia, SPAIN, email: joanda@die.upv.es

* Corresponding author.

Abstract— Structural defects in the rotor cage of large electrical machines significantly impact their expected operational lifetime. This work presents the results of simulating the thermal stresses developed in a rotor cage during a fatigue test in which a bar breakage was achieved. A combined model featuring electrical, thermal and mechanical stages as well as three different meshes reflecting a progressing narrowing of one of the bars in its junction to the end ring are used for this purpose. The experimentally implemented startup and plug stopping transients are reproduced as well as, for comparison, the stall operation. The resulting stress levels are in agreement with the progression of the damage and concur with the stator measurements. Based on the analysis of the simulated rotor magnitudes, a strategy to diminish the thermal stresses in a damaged cage is proposed.

Keywords— Finite element analysis, induction motors, prognostics and health management, rotors, thermal stresses, transient analysis.

NOMENCLATURE

Al	Aluminum
C	Elastic modulus tensor
Cp	Heat capacity
$\vec{d}$	Displacement field
EM	(Analytical) electromagnetic model
$\vec{f}$	External force

Fe Iron

FE Finite element model

h Heating power

I_r Rotor currents

I_s Stator currents

k Thermal conductivity

L_{rr} Rotor inductances

L_{sr} Stator-rotor mutual inductances

L_{ss} Stator inductances

LSH-50 Low Sideband Harmonic for the 50 Hz component

R_r Rotor resistances

R_s Stator resistances

$\vec{u}$ Unitary vector

U_s Stator voltages

β Thermal expansion tensor

ε Linear strain

ρ Charge density

ρ_d Mass density

ϕ Electric potential

σ Electrical conductivity

$\bar{\bar{\tau}}$ Stress tensor

Ψ_r Rotor flux linkages

Ψ_s Stator flux linkages

θ Temperature

1 INTRODUCTION

The rotor cage of an electrical motor is responsible for the conduction of the high currents whose interaction with the stator-generated magnetic flux yields the required torque. Built with aluminum or copper solid conductors, generally casted for smaller units and welded in large ones, this element comprises longitudinal bars attached at both ends to short circuit rings or plates (Fig. 1). It electrically behaves with respect to the stator as the secondary, having a low number of turns, of an electrical transformer,

hence the scale of the currents driven. Furthermore, due to the Faraday's law, their magnitude varies according to the difference, known as slip, between the turning speed of the field generated by the stator, fixed by the feeding voltages and its configuration, and the spin of the rotor. The higher the slip, the greater value $\partial\vec{B}/\partial t$ and hence the induced voltage in the cage. Thus, Direct-On-Line startups (DOL), the connection to the grid of a motor at standstill, constitute an especially burdensome event for this kind of machines. Values of current between 6 and 10 times the ones expected at rated operation are common during this transient even though, since the rotor is initially subjected to the grid's frequency, reactances limit the current inrush and the skin effect decreases the effective electrical section of the solid conductors.

Nevertheless, DOL startups are commonly used on large units in the industry not only for induction motors, but also as a way of accelerating the rotor of synchronous ones to a speed close enough to the field's one, due to the fact that Variable Speed Drives (VSD) and other ways of limiting the initial currents based in power electronics, such as starters, are either very expensive for the powers involved or its complexity prohibitively reduces the reliability of the whole system.

Therefore, the assessment of thermal stresses in the rotor cage of large motors, arisen mainly as a consequence of severe startup or stall transients (this later happens when the movement of the rotor is prevented by jamming), becomes an essential stage of its design. An example of this process is depicted in [1], where currents in the rotor cage are simulated by straightforward electrical per-phase model of the motor and then applied to thermal lumped models to calculate, considering adiabatic conditions, the expected temperature rise due to Joule heating. Skin effect is modelled considering a multilayer approach for the bars, focusing the heat generation on its top. The temperature profiles obtained feed a finite element (FE) linear elastic solver that yields an estimation of stresses caused by the thermal expansion of the material given the structural constraints of the element. These stresses are particularly important at the connection of the bars to the end ring. The input of its maximum value in a S-N diagram provides the number of cycles the machine can withstand, which should exceed what is established in the standards.

Ref. [1] portrays the complexity of the problem facing the manufacturers of predicting thermal stresses in the rotor cage during transients, involving the computation of electromagnetic, thermal and mechanical quantities –fully decoupled in that work–, the use of lumped parameter models whenever possible and the difficulties of validating the results in the actual operational conditions (there only the temperature rise in stall is compared with the values provided by the model).

In addition, this estimated theoretical performance deteriorates noticeably under anomalous conditions: vibrations [2], pulsating loads [3] and cage imperfections [4] can deeply decrease the rotor's cage expected lifetime. This later defect, which reduces the section able to conduct current in a solid conductor, involves large temperature gradients that cause thermal fatigue, showing an

evolution orders of magnitude faster [5]. Hence the interest of motor manufacturers for using copper in the construction of the cage rather than for an improvement in conductivity, due to its better mechanical characteristics and increased heat capacity [6].

The study of fatigue in rotor cages has also drawn the attention of several authors related to the mining industry, which reflects the relevance of the problem under the demanding conditions that motors are operated in such applications. Cabanas et al. in [7] pointed out the importance of thermal processes as a methodology to model a bar breakage (usually involving the detachment of the bar from the end ring) taking into account, as it is commonly done [8], only inertial forces under a high cycle fatigue approach, was unsuccessfully applied. However, Pitis in [9] used a full analytical approach to study the thermo-mechanical stresses that arise in weak points ("hot spots") of the rotor bars, specifically in the filament joining the external and internal rotor cages of a big motor (dual rotor cage motors are used to provide, due to the skin effect, a different behavior of the machine between startup and stationary operation). The full phenomena comprised in the Physics of Failure for low cycle fatigue damage are correctly identified in this work and applied to a 2D section of the motor. In addition, the temperature rise during several transients is compared.

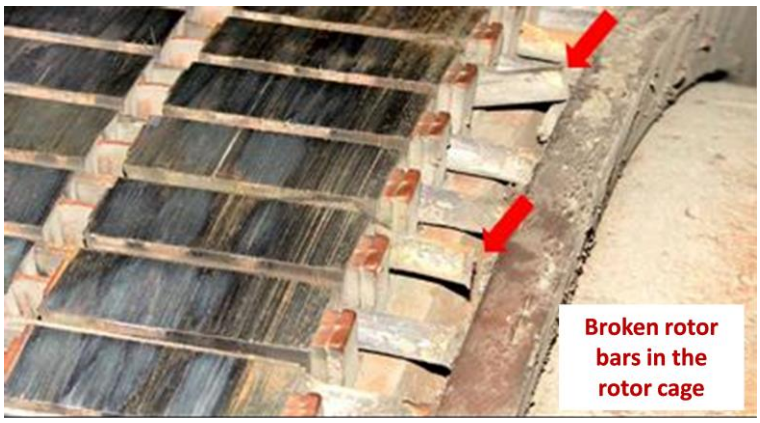

Fig. 1. Evidence of two broken bars in the rotor of an induction motor

Inspired by these developments, [10] proposed a combined approach (Fig. 2) to simulate the thermal stresses in a rotor cage caused by hot spots increasing a further step the integration of the electromagnetic, thermal and mechanical models. This is justified due to the stronger coupling of different phenomena under this anomalous operation mode. The electromagnetic behavior of the machine is calculated analytically and then the computed currents reproduced for each time step on a 3D mesh representing half of the rotor. The yielded current distribution in this mesh (only taking into account the resistances of the rotor elements) is used to obtain the heating and the temperature distribution, whilst thermal effects arising from magnetic phenomena were imposed on the mesh from independent analytical calculations. The computational requirements were reduced by modelling the stator and air regions of

the motor by a thermal network [11] since no such a detail was needed in these elements. Finally, stresses developed due to thermal expansion were computed on the cage mesh by a post processing stage.

The aim of this work is thus to use the model proposed in [10] to explore the thermo-mechanical conditions under which a bar breakage developed during a fatigue test [12] with the purpose of providing a mitigation strategy. This long experiment, spanning more than 80,000 cycles, was aimed at comparing signal analysis techniques applied to the stator currents to detect the incipient defect and track its evolution. Obvious limitations prevented employing a larger machine; therefore, the motor featured a cast aluminum cage and due to lack of clearance, no rotor quantities (besides rotational speed) were measured. As the bar breakage didn't develop, the cage structure was modified during the test. Firstly, two grooves were lathed in the end rings, in its junction with the rotor bars. Later, two drills were executed in one of the grooves next to one of the bars. In this manner, a structural configuration closer to the one used in large machines (cantilevered end ring and protruding bar) was achieved (see Fig. 3). The drills were widened effectively reducing the bar's section in a controlled and gradual way until the fault naturally developed [12].

Accordingly, the research line followed in this work consists of a posteriori analysis in which the combined model introduced in [10] is used to obtain from available data, recorded during the development of the fault, the non-measured variables, namely the rotor temperature and stress distributions, in order to ascertain corrective procedures. More specifically, since currents are much higher in the rotor cage during transient operation, this paper is thus focused on systematically studying the long startup and the plug stopping performed during the fatigue test with objective of finding stresses in the hot spot that are in agreement with the detailed evolution of a crack shown by stator current analysis in [12]. Besides that, given that the values of the convection coefficients in the model are linked to the mechanical speed of the machine, stall transients, considered the most damaging ones since there is no end space and air gap ventilation [13], are also easily simulated for comparison purposes by establishing in the movement equations of the rotor a load inertia high enough to avoid its turning. The progressing widening of the drills next to the bar executed during the last stage of the experimental test is reproduced here by using three different meshes in the simulations, featuring a bar's remaining section reduced to 12%, 8% and 4% of its original value, complementing the results of [10] in which just the latter was employed, and completing the ones presented in [14]. In this manner the full development of the fault can be depicted and the simulated results compared to the experimental ones published in [12], showing a good agreement despite all the assumptions made. A sensibility analysis regarding the interbar resistance parameter, difficult to measure or estimate, is also carried out in this work. Based on the analysis of this complete simulated results, a novel mitigation strategy, not included in [14], is developed.

For these purposes, the rest of the paper is organized as follows, Section 2 gives an overall description of the combined model used here, already introduced in [10], Section 3 shows the simulation's details, Section 4 presents the simulated results, further discussed and compared with experimental values in Section 5, and Section 6 yields the conclusions.

2 COMBINED MODEL

The stresses developed in a rotor cage during a transient arise as a result of the inertial forces produced by the rotation and angular acceleration of the rotor and the electromagnetic induced heating. In the latter case, their accurate computation, especially under asymmetric conditions (i. e. one of the bars is weakened) would yield a heavily coupled electromagnetic-thermal-mechanical problem. In order to avoid this, which would make the problem unapproachable, this work employs a taylored model (Fig. 2) developed in [10], built around the Elmer FE software [15] that assumes a direct coupling between distributed parameters in the rotor just for the variation of aluminum conductivity with temperature. Several other values needed in the FE computation, such as the boundary conditions and some body forces are calculated by ancillary functions programmed in FORTRAN solving Ordinary Differential Equations (ODE) with lumped parameters and called as required.

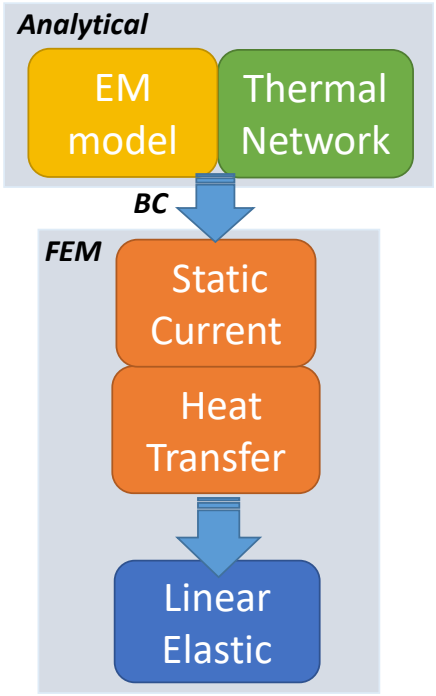

Fig. 2. Diagram of the combined model used for the simulation of the thermal stresses. Analytical models supply the boundary conditions and body forces for the coupled FE computation of the DC current and thermal state of the rotor. A post-processing by the linear elastic module yields the induced stresses.

A. Electromagnetic Model

The electromagnetic (EM) state of the machine (whose characteristics are presented in the Appendix) has been reproduced by means ODEs using the magnetic coupled circuits approach. Although not so accurate as FE analysis, the computation is much faster, reducing the time required for the combined model to perform a simulation by one order of magnitude. This EM model was specially designed for simulating faulty induction motors since treats independently each bar of the cage, and thus they can feature different resistances. It comprises a set of $m+n$ equations (with m stator and n rotor phases) in the form:

$$[U_s] = [R_s][I_s] + \frac{d[\Psi_s]}{dt} \tag{1}$$

$$[0] = [R_r][I_r] + \frac{d[\Psi_r]}{dt}. \tag{2}$$

The first equation models the stator winding (or primary circuit), fed by external voltage U_s, whereas the second reproduces the bars of the rotor cage connected between two neutral points. The flux linkages are defined as a linear combination of inductances in the form:

$$[\Psi_s] = [L_{ss}][I_s] + [L_{sr}][I_r] \quad (3)$$

$$[\Psi_r] = [L_{sr}]^T[I_s] + [L_{rr}][I_r] \quad (4)$$

In this kind of rotating electrical machine models the difficult part lies in how the coupling parameters among all the circuits, L, are obtained for each position of the rotor, which is especially burdensome if this computation cannot be simplified due to symmetries. Therefore, in this EM model, circular convolution is utilized to calculate this magnitude from the conductor's distribution along the airgap [16].

From the electromagnetic point of view, this approach is manifestly limited, since no iron saturation due to the high values of magnetic flux density is taken into account, it neglects the effect of the end rings connecting the rotor bars at their ends and doesn't provide magnetic variables to compute quantities such as iron losses. Nevertheless, it yields the variable heating source for each of the bars in the rotor cage in operation transients, which is the dominating effect during the fatigue test.

In order to couple this ODE model to the partial differential equations (PDE) of the mesh used for solving the DC current distribution in the rotor, half the voltage of the resistive term, $[R_r][I_r]$, in (2) is applied to the bars in the middle section of the half rotor shown in Fig. 3 e). Once the coupled DC electrical and thermal FE computations are performed, the resistance for each rotor bar in this EM model is updated proportionally to the ratio between the current in (2) and the current actually crossing those surfaces on the mesh. In this manner the progressing fault is reflected in the electromagnetic variables of the machine, acting the rotor thermal model acts as a surrogate to the study the rotor resistances, where distributed parameters are applied and then, when a solution is reached, the lumped values used in the electromagnetic one are updated.

B. Thermal Model

In order to focus the computational effort in the motor's region where it is mostly needed, PDEs are solved in the rotor mesh (Fig. 3 e) using the FE solver whereas, the rest of the rotor is modelled by a thermal network using ODEs [3, 11]. Both thermal models are weakly coupled by Neumann boundary conditions on the mesh (representing a heat flux) and the corresponding heat sources in the network divided in shaft, end ring and rotor iron surface.

The main heat source for the thermal model is computed by Elmer's static current conduction module solving the quasistatic approximation of the Maxwell equations. Since under these conditions, the curl of the Faraday's and the curl's divergence of

Ampere's laws are equal to zero, the electric scalar potential ϕ can be used to univocally compute the distribution of currents in the mesh [9]:

$$\nabla \cdot \sigma(\theta)\nabla\phi = \frac{\partial \rho}{\partial t} \qquad (5)$$

The distributed Joule heating is calculated from the electrical variables as:

$$h_{joule} = \nabla\phi \cdot \ \sigma(\theta)\nabla\phi \ . \qquad (6)$$

Once this value is obtained, the heat transfer module is called and used to solve the heat equation for θ with this later term as a distributed heat source *h*.

$$\rho_d c_p \left(\frac{\partial \theta}{\partial t} + (\vec{u} \cdot \nabla\theta) \right) - \nabla \cdot (k\nabla\theta) = \rho_d h \qquad (7)$$

Since the temperature the aluminum cage may change hundreds of degrees during the computation, (5)-(7) are strongly coupled in the rotor cage's regions by the parameter σ, the electric conductivity, which varies with temperature according to [17]. In the rotor's iron regions, however, σ is a second order constant tensor to take into account the negligible conductivity in the axial direction due to the effect of its laminated construction, designed to avoid eddy currents, being the values in the other two directions the corresponding to the interbar resistance assumed in [18]. The thermal conductivity *k* for the iron parts, a critical parameter, is treated in a similar way according to the values by [3]. Furthermore, in (7) ρ_d accounts for the mass density of the material and c_p for its heat capacity.

The approach for treating the magnetically-induced phenomena in the rotor mesh has been to compute the values externally using analytical functions and impose them on the mesh. Hence, a new heat source is added to (7) to account for the average iron losses, although its contribution during a transient is negligible (3.5% of the heat generation). The more significant skin effect in the rotor bars is approximated by modifying the heat capacity of the bars in its radial direction, according to the field frequency obtained from the electromagnetic model [10]. In this manner, the same amount of DC current produces higher temperatures at the top of the bar than at the bottom, reproducing the effect of an AC current. However, this strategy cannot be followed on the complex geometry of the end ring.

C. Linear Elastic Model

Elmer's Linear Elastic module, solving the dynamical equation for elastic deformation of solids (8) for the displacements in the mesh $\vec{d}$, is used as a post processing stage to obtain the effects on the cage produced by the heating:

$$\rho_d \frac{\partial^2 \vec{d}}{\partial t^2} - \nabla \cdot \bar{\bar{\tau}} = \vec{f} \quad (8)$$

$$\varepsilon = \frac{1}{2}\left(\nabla \vec{d} + \left(\nabla \vec{d}\right)^T\right) \quad (9)$$

where ε is the linear strain, $\vec{f}$ s volume force, and τ the stress tensor, computed as:

$$\tau^{ij} = C(\theta)^{ijkl}\varepsilon_{kl} - \beta^{ij}(\theta - \theta_0)\,. \quad (10)$$

In (10) C(θ) accounts for the temperature-dependent elastic modulus tensor, β is the thermal expansion tensor, in this particular case both reduced to scalars and θ_0 the reference temperature, which varies according to the transient studied, 316.9 K for cold startup and stall, 335 K in the case of cold plug stopping and 443 K for warm plug stopping. Tensile stresses arisen during the cooling process are not computed in this work.

3 SIMULATIONS

PDEs for assessing the thermal and mechanical state of the rotor are solved in the three different meshes shown in Fig. 3. They depict just half of the induction's motor rotor with the objective of providing a point (the middle sections of the bars) where the resistive potential calculated by the EM model can be applied. Their construction is symmetric, albeit the narrowing created at the junction of one of the bars to the end ring, whose cross section is varied modifying the centers of the drills and their diameter. This reproduces the machining process carried out during the fatigue test [12] to weaken one of the bars, first to an estimated 14 % of its total cross section (Fig. 3 b)) and then up to 7 % (Fig. 3 a)). In this experiment a small evolution of the fault indicators was observed for the first case and a rapid one, comprising a few hundred cycles until full breakage, for the second. Therefore, in order to explore that range, the geometries used in the simulation have a remaining section of 4% (Fig. 3 c), also utilized in [10]), 8% (Fig. 3 d)) and 12% (Fig. 3 e). Further, Table I depicts the main parameters common to the computations.

TABLE I. PARAMETERS OF THE SIMULATIONS

Voltage	400 V	**$\sigma_{x,y}$ (Fe)**	1.67 10^3 S
Frequency	50 Hz	**σ_z (Fe)**	0
Inertia, J	0.13 kg·m^2	**$k_{x,y}$ (Fe)**	31 W/m·K
External Temperature	297 K	**k_z (Fe)**	0.6 W/m·K
Time step, EM model	$1 \cdot 10^{-6}$ s	***k* (shaft)**	31 W/m·K
Time step, FE model	$1 \cdot 10^{-3}$ s	***Cp* (Fe, shaft)**	449 J/kg K
***Cp* (Al)**	897 J/kg K		

Regarding the operational conditions used in the simulations, this study is focused on the transients experienced by the machine during the fatigue test, when currents are higher. Therefore, according to the experimental procedure of [12], in which the cycling consisted of a heavy startup transient, lasting up to 7 seconds, a stationary (constant rotational speed) period of 13 seconds and an even heavier plug stopping of around 5.5 seconds, followed by a cooling down interval, startups and plug stoppings on the meshes reflecting different sizes of the rotor were reproduced in this work. Additionally, since in the combined model all the convection coefficients are speed-dependent, stall transients have also been simulated just by inputting a very high inertia in the EM model, effectively preventing any movement in the rotor as it happens in the industry when the load is jammed. Table II summarizes all the cases studied. Compared to [14], further simulations using the 12% mesh have been carried out for the plug stopping and stall operation.

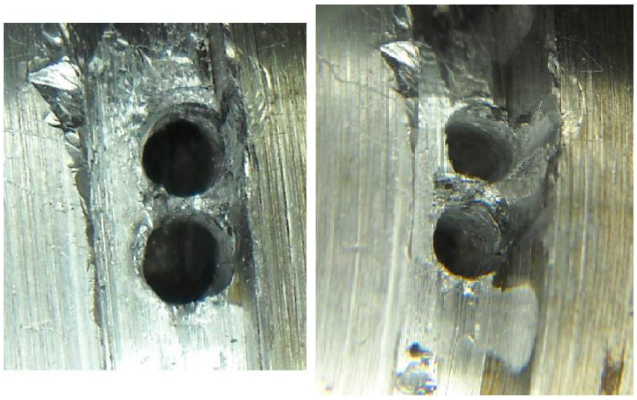

a) b)

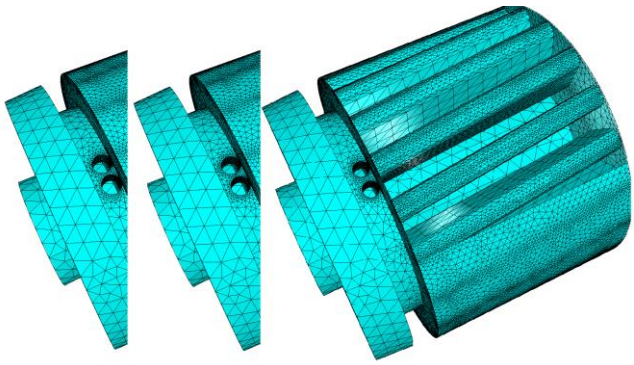

c) d) e)

Fig. 3. Weakening of the bar carried out in [12] with an estimated remaining section 7 %, a) and 14 % b) (top). Meshes used to compute the thermal and mechanical state of the rotor showing different remaining section of the bar: 4% c), 8% d) and 12% e) (bottom).

TABLE II. CASES STUDIED AS PERCENTAGE OF THE REMAINING BAR CROSS SECTION

Operation Mode	**Initial thermal condition**	
	Cold	**Warm**
Startup	4, 8, 12 %	-
Stall	4, 8, 12 %	-
Plug stopping	4, 8, 12 %	4, 8, 12 %

Furthermore, for the initial conditions, given the cycling in [12], during the plug stoppings temperature gradients in the motor exist. Thus, an initial thermal state of the rotor bodies in the mesh and the thermal network depicting the rest of the motor is necessary to begin the time-stepping simulation. Therefore, initial values have been obtained running a full thermal network (depicting also the rotor) according to the cycling carried out during the fatigue test, up to the point when the plug stopping was switched on in [12]. Uniform temperature almost at equilibrium with the ambient was used for the rest of the simulations, as experimentally assessed [10].

4 RESULTS

This section presents a comparison among the results of the previous 12 cases simulated, which on average took in a PC one day for each second of the simulation computed.

D. Cold Startup Cases

Fig. 4 a) shows the average temperature evolution along a radial line centered in the narrowest part of the hot spot during the startup transient, for cold conditions. The reduction of the section of the bar from 12% to 8% rises the maximum temperature from 370.7 K to 378.7 K, but maintains the shape of the curve, peaking both at 3.5 s. Nevertheless, when the fault progresses further to 4% the increase of resistance limits this value to 374.8 K and maintains it for around one second (3.5-4.5 s), following a more irregular pattern. The averaged maximum temperature rise in all the cases is 57.8 K.

Subsequently, Fig. 4 b) depicts the maximum Von Mises stress on the surface of the hot spot as well as (dashed lines) the computed yield stress limit of aluminum for the temperatures and severity of the defect presented in Fig. 4 a). The wider shape of the saddle maintains the Von Mises stress clearly below the yield limit (σ_Y) for the 12% remaining bar section case, despite the similar temperature increases. The 4% and 8% the curves, however, approach plastic deformation conditions and, in the former case, surpass it between 2-4 s. This plastic deformation would trigger a low cycle process and therefore a progressive deterioration of the remaining section of the bar.

E. Plug Stopping Cases

The temperature evolution in the hot spot for the other transient implemented in the fatigue test, the plug stopping, is shown in Fig. 5 a) grouped in two sets: cold plug stopping, having an initial temperature of 335 K and warm plug stopping, starting at 443 K. All were simulated for the 4%, 8% and 12% sizes of the defect.

The heating profile of the hot spot is simpler compared to the startup case, resembling a first order system evolution, due to the higher warming rate and decreasing convection coefficients. A stepper rise in the first instants, is followed by a stabilization afterwards, reflecting the effect of the decreasing currents as the rotor decelerates and the difference with the field rotation, now spinning in the opposite sense, is reduced. The 4% and 8% cases evolve similarly after connection but higher temperatures, around 25 K are obtained as the transient progresses for the later. The average temperature increase is 96.6 K for the cold simulations and 93.7 K for the warm ones. Alike to the startup transient, the 12% simulations initially show a lower temperature rise, but in these cases is followed by a higher heating rate.

Fig. 5 b) presents the Von Mises stress obtained at the surface of the hot spot for the cases whose temperature is shown in Fig. 5 a), as well as the yield limit of aluminum at the temperature of the least severe of them (the values for the rest of the transients are lower). It can be appreciated how the temperature rise in the first quarter of a second exhausts the elastic properties of this material for the narrowest sizes of the defect (4 %, 8 %). Afterwards, the maximum simulated stresses stabilize above around 65% of the yield limit, between 35 and 40 MPa, following the temperature's trend due to the reduction of currents in the bars as the rotor decelerates. Less stresses, around 30 MPa, peaking at the end of the transient are obtained for the 12% cases. This late rise is similar to the one observed for the startup.

F. Stall Cases

Fig. 6 a) shows the simulated temperature rise of the hot spot during a stall transient for the three meshes. The overall pattern is analogous to the previous case, showing the characteristic first order system evolution with higher temperatures for a remaining section of the bar of 8%. Stresses increase in a similar way as temperatures (Fig. 6 b) for this case but the simulations of 12% and 4% stay below the yield limit several seconds after connection. From the study of the three previous operation modes shown in Fig. 4-6, it can be stated that there is a critical size of the defect that, depending on the electrical loads and thermal configuration of the cage, yields the highest temperature increase and that for this motor is 8%. However, this may not directly translate into more severe damage due to structural factors (the size of the saddle between the drills) that allow the accommodation of the material's expansion without increasing the stress level.

It is also worth to mention the differences between the cold start 4% case in Fig. 4 and stall 4% one in Fig. 6. Higher temperatures and stresses appear in the first one, depleting the elastic properties of aluminum just after 1.5 s, whereas in Fig. 6 b) it is clearly shown that for stall this happens at 3.5 s, when the Von Mises stress in the saddle surpasses the elastic limit of the material. This is caused by the skin effect, since during stall conditions the heating is more intense at the top of the bars, but the hot spot is situated at the bottom of one of them (Fig. 3), thus effectively improving the cooling in that case. During the cold startup, however, due to the reduction of frequency in the rotor currents, the bar warms up more evenly and thus the hot spot is facing higher temperatures from that side. Therefore, this different behavior is a particular effect caused by the geometry and not a generalizable result.

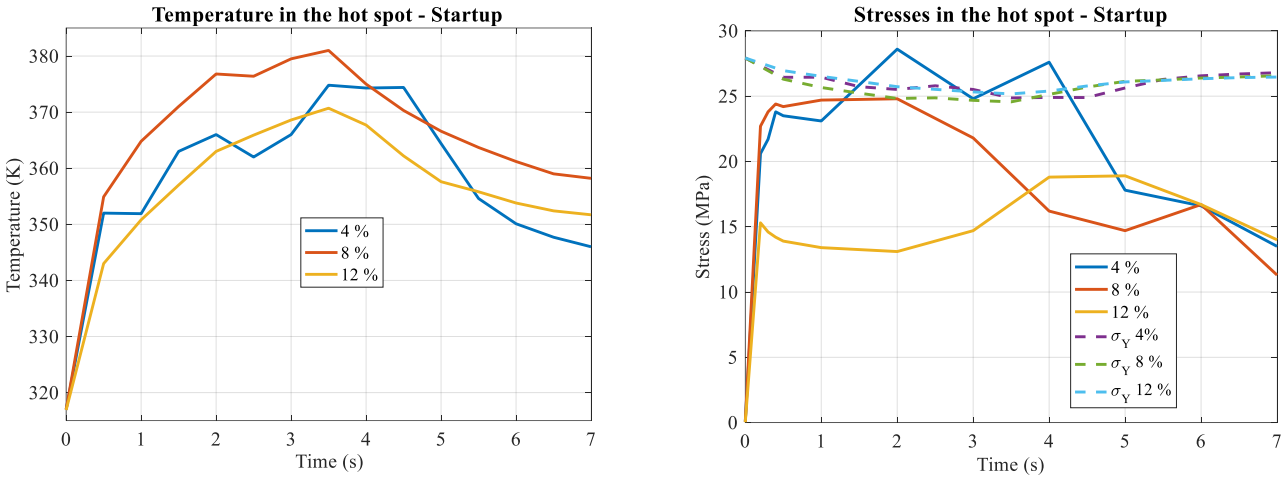

(a) (b)

Fig. 4. Temperature evolution in the hot spot during the startup transients (a) and stresses developed (b).

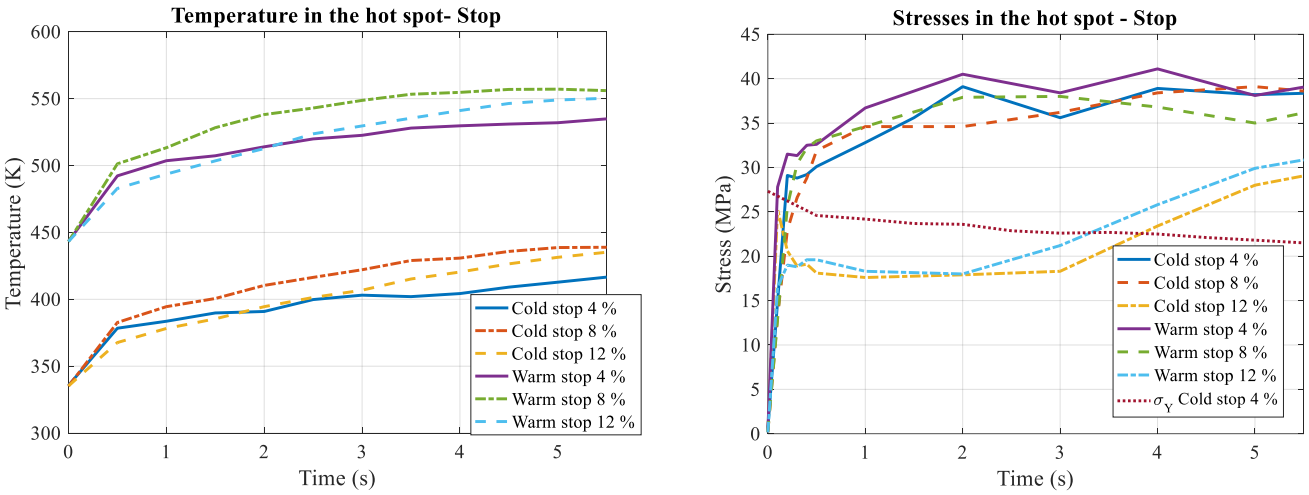

(a) (b)

Fig. 5. Temperature evolution in the hot spot during the plug stopping transient (a) and stresses developed (b).

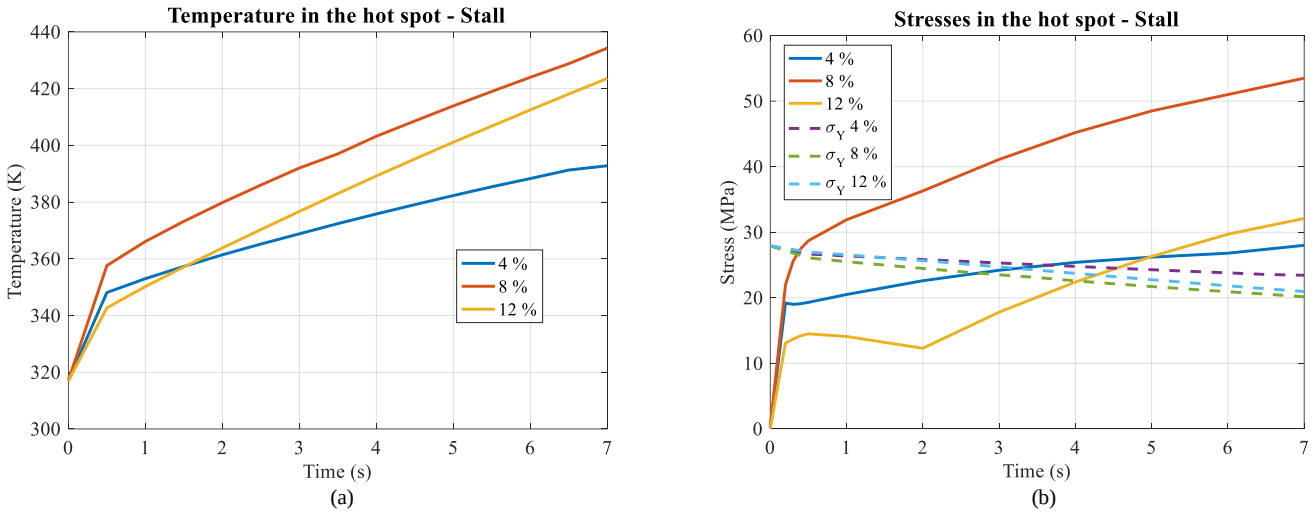

(a) (b)

Fig. 6. Temperature evolution in the hot spot during the stall transient (a) and stresses developed (b).

5 DISCUSSION

In this Section the previous simulations are discussed, compared to experimental data and a mitigation procedure is proposed.

G. Agreement with Experimental Results

The modelling of the stator using electromagnetic and thermal ordinary differential equations permits linking the FE simulations of the rotor carried out in this work to external magnitudes of the machine recorded during the fatigue test in [12] in a computational efficient way. Their comparison yields an indication of the performance of the model even though rotor stresses themselves were not measured during the test.

Contrary to [10] and complementing [14] with further simulations, in this work the study of three different meshes showing the development of the fault allows checking the resemblance of the evolution of electromagnetic quantities as the fault progresses (thermal ones don't differ from the case shown in [10]). Transient current analysis is employed on the stator currents to obtain an accurate quantification of the rotor cage asymmetry for the startup cases, both from the current waveforms yielded by the model in the simulations and from the recorded experimental results, by tracking an integrating the energy in the LSH-50 harmonic during the transient and normalizing it with the one from the main current component. This sideband increases its amplitude for a single defect as the bar section is reduced. The results of computing the Wigner-Ville based indicator, γ_W (Eq. 5 in [12]), are presented in Table III, in which the simulated values are compared with the values obtained during the fatigue test and the ones from a third motor of the same characteristics. In this latter case no cold startup waveforms were available.

Despite of the several assumptions made building the combined model, the simulated values roughly lie between the healthy (100 % remaining bar) and broken (0 % bar) states, even though real machines always exhibit a constructive rotor asymmetry, which in the case of the fatigue test (Experimental I motor in Table III) is initially compensated by the developing fault [19].

TABLE III. ROTOR ASYMMETRY HARMONIC ENERGY DURING STARTUP FOR DIFFERENT SIZES OF DEFECT

Simulated		**Experimental I (Fatigue test)**		**Experimental II**	
Size	**γ_w (dB)**	**Size**	**γ_w (dB)**	**Size**	**γ_w (dB)**
-	-	100 %	52	100 %	54.3*
12 %	54.4	14 %	56	-	-
8 %	50.9	7 %	47	-	-
4 %	49.1	-	-	-	-
-	-	0 %	34	0 %	34.4*

*Warm startup, from [12].

The evolution of the experimental indicators is wider compared to the simulated ones, as it can be seen in Fig. 7. During the fatigue test a reduction from an estimated 14% to 7% by increasing the diameter of the drills half a millimeter produced a descent (worsening) in the asymmetry indicator of 9 dB, whereas in the simulated case is just 3.5 dB. This trend increases as the fault progresses. Overall, the model damps the asymmetry. Several causes may justify this behavior such as the effects of saturation, which are not modelled, the connection of the rotor bars in the EM model, or a low value of the considered interbar resistance. To assess the impact of this later parameter, which is difficult to measure on a real machine and even changes during its lifetime reflecting the thermal history of the rotor, a sensitivity analysis for the cold startup simulation and a section of the bar equal to 8% was repeated for other resistance values. The results are shown in Fig. 7 and Table IV:

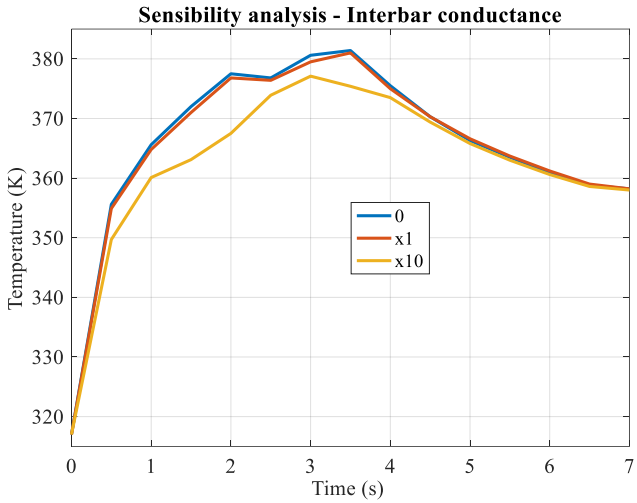

Fig. 7. Temperature increase during the cold startup in the case of 8% remaining section of the bar for different values of interbar conductance.

TABLE IV. MAXIMUM TEMPERATURE DURING THE COLD STARTUP, 8% CASE

Interbar conductivity	**θ at 3.5 s (K)**
0	381.4
1.67 10^3 S	378.7
1.67 10^4 S	375.4

Since the silicon iron's conductivity is orders of magnitude lower, as long as it still exist a sizeable aluminum path for the conduction of currents, the portion of the current diverted through the iron doesn't reach values that impact the result of this work even under variations of interbar resistance of 1 to 1.5 orders of magnitude.

Regarding the simulated thermal stress values presented in the previous section, a qualitatively agreement with the evolution shown by the experimental data acquired during a fatigue test in [12] is observed. According to the simulations, for this machine and operating conditions the reduction of the cross section of one bar must be below 15 % to trigger a low cycle fatigue process, as the thermal stress in the hot spot surpass the yield limit of aluminum in the plug stopping stage (Fig. 5 b)). This would explain the slow evolution observed in the experiment when the bar's area was reduced to 14 % of its actual size (Fig. 8). Around 8 % a second stage is reached, as the maximum thermal effects take place, which again corresponds in the fatigue test to the size when the bar breakage

rapidly developed in the test (Fig. 8). Finally, as the remaining section of the bar is further reduced, the amount of current through it decreases and accordingly the temperature of the hot spot, although stresses remain high until the full breakage happens.

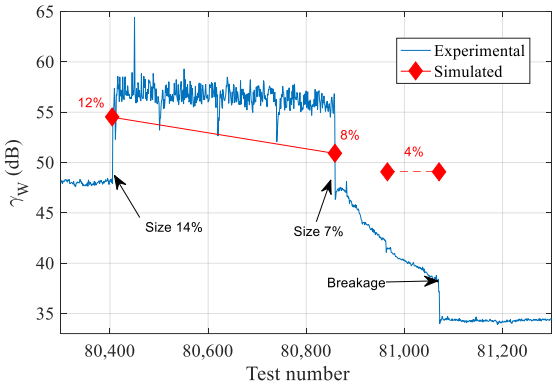

Fig. 8. Evolution of the rotor asymmetry indicator during the fatigue test of [12] (blue), and values corresponding to simulated sizes of the defect (red diamonds). The position of the size 4% is estimative.

H. Proposed Mitigation strategy

It is noticeable comparing Fig. 5 and 6, for the 8% remaining bar case at, for instance, 5 s into both transients, that for the same temperature raise in the hot spot, 103.7 K in the plug stopping and 97 K in the stall case, the maximum stresses developed in the saddle are 39.1 MPa in the former and 48.5 MPa in the later simulation (Fig. 5 b) and Fig. 6 b)). Measured on the mesh, the difference of temperature between the hot spot and the end ring facing it is 13 K for the plug stopping and 19.7 K for the stall. This greater thermal gradient would explain the increase of 24% in the damage produced in the later transient.

Furthermore, Fig. 9 shows the difference between temperature increases during both transients:

$$\Delta\theta = (\theta_{5s} - \theta_0)_{stop} - (\theta_{5s} - \theta_0)_{stall} \,. \qquad (12)$$

Despite a difference of 7 K in the hot spot, the end ring features an average of roughly 12.5 K, and 13.8 K variation in the section immediately facing the defect; therefore, it has been warmed up comparatively more in the plug stopping case, reducing the temperature gradient with the hot spot. This may be explained by the evolution of the current during the transients: reversing the sequence of currents to halt the motor cause higher initial values, followed by a gradual reduction, whereas for the stall transients remains overall constant, being only affected by the slowly increase of the conductors' resistance in rotor and stator (Fig. 10). These higher initial currents in the rotor cage warm both defect and end ring, but since the heat transfer from the later is limited, higher

temperatures remain in that part of the cage during the rest of the transient, damping the temperature gradient to the hot spot as it warms up and causing the maximum stresses to remain lower and fairly constant compared to the stall case (Fig. 5 b)).

Therefore, the stresses developed in damaged rotor cages due to thermal expansion during heavy transients could be limited by preheating some components taking advantage of their different heat transfer characteristics and electrical configuration inside the machine.

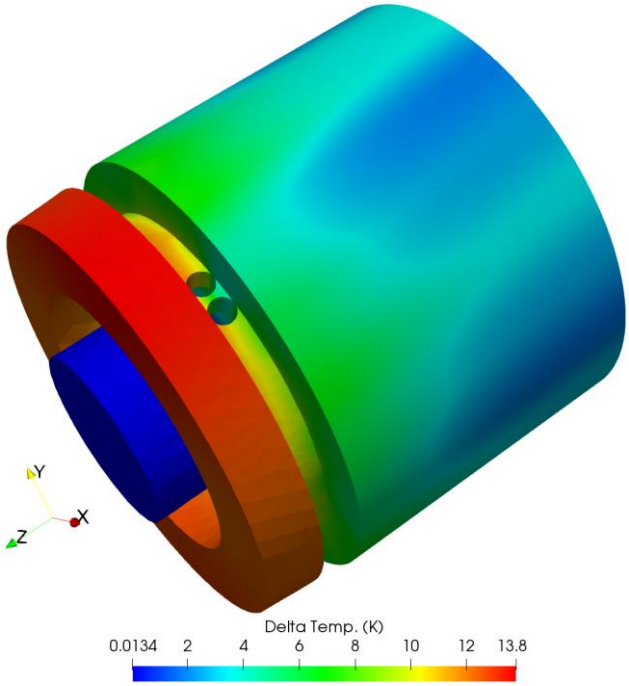

Fig. 9. Difference of temperature rise between the plug stopping transient and the stall transient after 5 s of simulation for a size of defect of 8%. In the first case the higher initial currents rapidly heat up the end ring well above the temperature increases of the rest of the rotor.

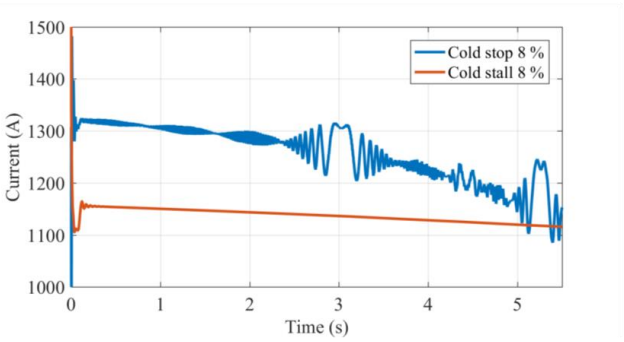

Fig. 10. Instantaneous amplitude of the currents in the bar facing the hot spot for the transients compared in Fig. 9.

6 CONCLUSIONS

An electromagnetic-thermal-mechanical combined model, weakly coupling most of the magnitudes involved, is able to provide results in agreement with the experimental evolution obtained during a fatigue test, explaining the progression of a bar breakage. Although some limitations still persist, such as the inclusion of saturation in the model, the proposed combined approach seems a promising way to study this failure and providing the evolution of all the involved variables. The simulations have shown the existence of a critical size of the defect that causes the greatest damage and, based on them, a mitigation strategy in order to limit the damage in faulty cages is proposed: using the different thermal and electrical characteristics of its elements with the aim of reducing the thermal gradients during the transients.

7 APPENDIX

Motor characteristics: Star connected, rated voltage (U_n): 400 V, rated power (P_n): 1.5 kW, 1 pole pairs, stator rated current ($I1_n$): 3.25 A, rated speed (n_n): 2860 r/min.

REFERENCES

[1] R. Yabiku, R. Fialho, L. Teran, M. E. Ramos, N. Kawasaki, “Use of thermal network on determining the temperature distribution inside electric motors in steady-state and dynamic conditions,” *IEEE Trans. Ind. Appl.*, vol. 46, no. 5, pp. 1787-1795, Sep./Oct., 2010.

[2] C. Bruzzese; A. Tessarolo; E. Santini, “Failure root-cause analysis of end-ring torsional resonances and bar breakages in fabricated-cage induction motors,” *in Proc. of ICEM 2016*, Lausanne, Switzerland, Sept. 4-7 2016, pp. 2251 – 2258.

[3] Design of Rotating Electrical Machines, J. Pyrhönen, T. Jokinen, V. Hrabovcová, Edt. Wiley, second edition, 2014.

[4] R. Yabiku, R. Fialho, L. Teran, A. Santos, E. Rangel, D. Dutra, "A comparative study between copper and aluminum induction squirrel cage constructions," *in Proc. Petroleum and Chemical Industry Conference (PCIC)*, San Antonio, TX, USA, Sept. 20-22 2010, pp. 1-9.

[5] S. Pietranico, S. Pommier, S. Lefebvre, S. Pattofatto, Thermal fatigue and failure of electronic power device substrates, *International Journal of Fatigue*, Volume 31, Issues 11–12, 2009, Pages 1911-1920,

[6] M. Hodowanec, W. R. Finley, "Copper versus aluminum-which construction is best? [Induction Motor Rotors], *IEEE Ind. Appl. Magazine*, vol. 8, 2002, pp. 14-25.

[7] M. F. Cabanas, J. L. Ruiz Gonzalez, J. L. B. Sampayo, M. G. Melero, C. H. Rojas, F. Pedrayes, A. Arguelles, J. Vina, "Analysis of the fatigue causes on the rotor bars of squirrel cage asynchronous motors: Experimental analysis and modelling of medium voltage motors," in Proc. SDEMPED, 2003, Stone Mountain, GA, USA, pp. 247–252.

[8] B. Bode, A. Brueckner-Foit, F. Zeismann, Quasi-static and cyclic failure behavior of electric sheet material, *International Journal of Fatigue*, Volume 82, Part 2, 2016, Pages 350-360,

[9] C. D.Pitis, "Thermo-mechanical stresses of the squirrel cage rotors in adverse load conditions," *in Proc. ISEI*, 2008, pp. 579-585, Vancouver, BC, Canada.

[10] V. Climente-Alarcon, D. Nair, R. Sundaria, J. Antonino-Daviu, A. Arkkio, "Combined model for simulating the effect of a heavy transient on a damaged rotor cage," *IEEE Trans. Ind. Appl.*, Vol. 53, nº 3, pp. 2040-2048, May-Jun. 2017.

[11] P. H. Mellor, D. Roberts, D. R. Turner, "Lumped parameter thermal model for electrical machines of TEFC design," *IEE Proceedings B - Electric Power Applications*, vol. 138, no. 5, pp. 205 – 218, Sept. 1991.

[12] V. Climente-Alarcon, J. A. Antonino-Daviu, E.G. Strangas, M. Riera-Guasp, "Rotor-Bar Breakage Mechanism and Prognosis in an Induction Motor," *IEEE Trans. Ind. Electron*., vol. 62 , no. 3, pp. 1814-1825, Mar. 2015.

[13] V. T. Buyukdegirmenci, P. T. Krein, "Induction Machine Characterization for Short-Term or Momentary Stall Torque," *IEEE Trans. Ind. Appl.*, vol. 51, no. 3, pp. 2237–2245, May-Jun. 2015.

[14] V. Climente-Alarcon, A. Arkkio, J. A. Antonino-Daviu, "Comparison of Thermal Stresses Developed during Transients on a Damaged Rotor Cage," *in Proc. ECCE, 2017*, Cincinnati, OH, USA, 2017, pp. 3545-3551

[15] Elmer Finite Element Software, CSC – IT Center for Science, FINLAND, [online], Available: https://www.csc.fi/web/elmer

[16] M. Pineda-Sanchez, V. Climente-Alarcon, R. Riera-Guasp, R. Puche-Panadero, J. Pons-Llinares, "Enhanced Simulink induction motor model for education and maintenance training," *Journal of Systemics, Cybernetics and Informatics*, Vol. 10, No. 2, 2012, Available: http://www.iiisci.org/journal/CV$/sci/pdfs/HEB064IU.pdf

[17] P. D. Desai, H. M. James, C. Y. Ho, “Electrical Resistivity of Aluminum and Manganese,” J. Phys. Chem. Ref. Data, Vol. 13, No. 4, 1984.

[18] N. Christofides, “Origins of load losses in induction motors with cast aluminium rotors,” *Proc. of the Institution of Electrical Engineers*, vol. 112, no. 12, pp. 2317 – 2332, 1965.

[19] M. Jeong, J. Yun, Y. Park, S. B. Lee, K. N. Gyftakis, “Quality Assurance Testing for Screening Defective Aluminum Die-cast Rotors of Squirrel Cage Induction Machines,” *IEEE Trans. Ind. Appl., (*doi: 10.1109/TIA.2018.2805828)